



HAL
open science

Computation of the radiation force exerted by the acoustic tweezers using pressure field measurements

Dan Zhao, Jean-Louis Thomas, R. Marchiano

► **To cite this version:**

Dan Zhao, Jean-Louis Thomas, R. Marchiano. Computation of the radiation force exerted by the acoustic tweezers using pressure field measurements. *Journal of the Acoustical Society of America*, 2019, 146 (3), pp.1650-1660. 10.1121/1.5126095 . hal-02325354

HAL Id: hal-02325354

<https://hal.sorbonne-universite.fr/hal-02325354>

Submitted on 11 Dec 2023

HAL is a multi-disciplinary open access archive for the deposit and dissemination of scientific research documents, whether they are published or not. The documents may come from teaching and research institutions in France or abroad, or from public or private research centers.

L'archive ouverte pluridisciplinaire **HAL**, est destinée au dépôt et à la diffusion de documents scientifiques de niveau recherche, publiés ou non, émanant des établissements d'enseignement et de recherche français ou étrangers, des laboratoires publics ou privés.

**Computation of the radiation force exerted by an acoustic tweezers using pressure
field measurements**

Zhao Dan,^{1,2} Jean-Louis Thomas,¹ and Régis Marchiano²

¹*Sorbonne Université, CNRS, Institut des NanoSciences de Paris, INSP,
F-75005 Paris, France*

²*Sorbonne Université, CNRS, Institut Jean Le Rond d'Alembert, ∂' Alembert,
F-75005 Paris, France*

1 Acoustic tweezers allow to manipulate small objects like elastic spheres with a force
2 generated by the radiation pressure which arises from the nonlinear interaction be-
3 tween the incident and scattered waves by the object. The accurate control of
4 the object by acoustic tweezers requires the study of the components of the three-
5 dimensional force. If the physical properties of the elastic sphere are known, then the
6 3D components of the force can be calculated thanks to a decomposition of the in-
7 cident acoustic field in the spherical functions basis. In this work, we propose to
8 evaluate the expansion coefficients. Three methods are used and compared. The first
9 one consists in measuring the acoustic field on a spherical surface centered on the
10 theoretical position of the object and to calculate the spherical functions decompo-
11 sition by Lebedev quadratures. The second method is based on the measurement of
12 the acoustic field at random points in a spherical volume and on the resolution of the
13 inverse problem by a sparse method called the orthogonal matching pursuit. In the
14 third method, the incident beam is measured on a transverse plane, decomposed into
15 a sum of plane waves and then the expansion coefficients are calculated. The results
16 of the three methods will be presented and compared.

17 I. INTRODUCTION

18 Acoustic tweezers like optical and magnetic tweezers are used for 3D manipulation of
19 small objects such as cells and molecules. These micro manipulators are in a strong demand
20 in the field of biophysics. Among these tweezers, optical tweezers¹⁻³ have been developed
21 first and demonstrated their precision and trap capabilities. However, the high intensity
22 at the focus of optical tweezers can lead to photo-damage and heating of the target ob-
23 ject, especially in vivo samples. Magnetic tweezers are not limited by photo-damage and
24 are widely used in the biology field especially for manipulation and analyses of DNA and
25 RNA^{23,32}. The main limitation of magnetic tweezers is the limited range of constant-force
26 that can be exerted due to their low trap stiffness. Moreover, applying large force requires
27 high-current electromagnets which would cause heating or produce non constant-force. The
28 radiation force is proportional to the field intensity divided by the speed of propagation.
29 As the velocity of light is 5 orders of magnitude larger than sound speed, acoustic tweezers
30 are able to afford large forces with much smaller intensity than optical tweezers and are a
31 solution for the heating issue. This advantage enables a wide range of applications of acous-
32 tic tweezers in various domains such as materials science, study of biophysical properties of
33 cells and molecules, micro-rheology, biophysical characterization of DNA, etc.

34 Different kinds of acoustic traps exist. Most of them are based on standing waves either
35 in the bulk³⁵ or propagating at the surface of a solid substrate^{13,14}. In these schemes, all
36 pressure nodes (or anti-nodes depending on the object density and compressibility) act as
37 potential traps. On the contrary, optical tweezers are selective traps with a single position

38 of equilibrium. Radial selectivity was achieved by Wu³⁴ using two counterpropagating fo-
39 cused ultrasonic beams. Single beam acoustic tweezers are characterized by the ability to
40 pick up, trap and manipulate a single small elastic particles in three dimensions^{4,5,7,9} as its
41 optical counterpart. For all the possible applications, the calibration of the force provided
42 by acoustic tweezers is of importance, especially for micro-rheology studies. The optical
43 and magnetic tweezers' forces calibration is achieved mainly by two methods: the first one
44 consists in studying the Brownian motion of trapped objects with sizes comparable to the
45 wavelength, then the force is determined from Hooke's law^{12,24}; the second one is to use the
46 viscous drag force generated by a controlled fluid flow²⁵.

47 Nonetheless, the first method is not applicable for acoustic tweezers since the wavelength
48 and the object can be much larger and the Brownian motion disappears at these scales. As
49 for the second method, the fluid drag forces are also used to calibrate the acoustic trapping
50 force²², but difficulties arise for single beam acoustic tweezers due to the Magnus effect¹⁶
51 caused by the rotation of bead in an acoustic vortex beam⁸. Previously, the three dimen-
52 sional force exerted on a spherical particle was modeled using the incident beam expansion
53 on spherical functions. This model depends on the expansion coefficients, A_n^m , dubbed beam
54 shape coefficients (BSC), and the scattering coefficients of the particle, R_n ⁶.

55

56 In this article, we are interested in characterizing the radiation pressure exerted by acous-
57 tic tweezers on a spherical particle using this model. Thus, this is not a direct measurement
58 of the force. The acoustic field is measured with a calibrated hydrophone and then the force
59 is deduced. Section II is a short reminder of the model focused on the equations needed

60 to calculate the radiation pressure exerted on an elastic sphere. To obtain the BSC of
61 the incident pressure field, three methods are numerically investigated in section III: Lebe-
62 dev quadrature, inverse problem regularization by sparsity and angular spectrum method
63 (ASM). In section IV, a focused Gaussian beam and a focused acoustic vortex are synthe-
64 sized and measured. The BSC are recovered by applying the three methods. Then, the
65 acoustic field is reconstructed and compared with measurements and finally the radiation
66 pressure is determined by the three methods.

67 II. THEORETICAL BACKGROUND: RADIATION PRESSURE

68 Let us consider a 3D Cartesian system of coordinates (x, y, z) . The three components of
69 radiation pressure exerted on an arbitrarily located elastic sphere in a perfect fluid by an
70 arbitrarily incident beam are⁶:

$$F_x = -\frac{\langle V \rangle}{k_0^2} \sum_{n=0}^{\infty} \sum_{|m| < n} \Im(Q_n^{-m} A_n^{m*} A_{n+1}^{m-1} C_n + Q_n^m A_n^m A_{n+1}^{m+1*} C_n^*), \quad (1)$$

$$F_y = +\frac{\langle V \rangle}{k_0^2} \sum_{n=0}^{\infty} \sum_{|m| < n} \Re(Q_n^{-m} A_n^{m*} A_{n+1}^{m-1} C_n + Q_n^m A_n^m A_{n+1}^{m+1*} C_n^*), \quad (2)$$

$$F_z = +2\frac{\langle V \rangle}{k_0^2} \sum_{n=0}^{\infty} \sum_{|m| < n} \Im(G_n^m A_n^{m*} A_{n+1}^m C_n). \quad (3)$$

With :

$$V = p_0^2 / (4\rho_0 c_0^2),$$

$$C_n = R_n^* + R_{n+1} + 2R_n^* R_{n+1},$$

$$Q_n^m = \sqrt{(n+m+1)(n+m+2)} / \sqrt{(2n+1)(2n+3)},$$

$$G_n^m = \sqrt{(n+m+1)(n-m+1)} / \sqrt{(2n+1)(2n+3)}.$$

71 $p_a(x, y, z, t)$ is the linear component of the acoustic pressure, its time average is zero. ρ_0
 72 and c_0 are respectively the fluid density and speed of sound at rest. Coefficients A_n^m are the
 73 coefficients of the expansion into spherical functions:

$$p_a(r, \theta, \varphi, t) = p_0 \sum_{n=0}^{\infty} \sum_{|m| < n} A_n^m j_n(kr) Y_n^m(\theta, \varphi) \exp(-i\omega t) \quad (4)$$

74 where the spherical harmonics are defined by:

$$\begin{aligned} Y_n^m(\theta, \varphi) &= \sqrt{\frac{(2n+1)(n-m)!}{4\pi(n+m)!}} P_n^m(\cos\theta) e^{im\varphi} \\ &= N_n^m P_n^m(\cos\theta) e^{im\varphi} \end{aligned} \quad (5)$$

75 with (r, θ, φ) the spherical coordinates linked to the Cartesian coordinates by $x = r \sin\theta \cos\varphi$,
 76 $y = r \sin\theta \sin\varphi$ and $z = r \cos\theta$. j_n designates the spherical Bessel function, $P_n^m(\cos(\theta))$ are
 77 the Legendre polynomials and k is the wave number. The azimuthal number m and the
 78 radial degree n satisfy $|m| \leq n$.

79 From the theoretical expressions of the radiation pressure, two sets of coefficients are required
 80 to determine the forces:

81 • Scattering coefficients: R_n

82 • Incident BSC: A_n^m

83 The scattering coefficients R_n for an arbitrary incident beam are known and depend only
84 on the physical characteristics of the object and propagation medium⁶. Therefore, our
85 problem of determining the radiation forces can be solved by searching the incident BSC
86 A_n^m . These coefficients are known analytically for several beams (plane wave, Bessel beam,
87 vortex beam). Nevertheless, in real applications the pressure field is sampled in time and
88 in space on a finite set of points and make the determination of BSC a challenge. In the
89 following part, three different methods for calculating these coefficients are investigated.

90 III. CALCULATION OF BEAM SHAPE COEFFICIENT A_n^m FROM THE PRES- 91 SURE FIELD

92 For each method, the determination of the BSC is tested on the same incident field: a
93 focused vortex beam of topological charge $m' = 1$. This beam is very important because,
94 it is the keystone to create acoustic tweezers^{4,5,7,28}. As this paper proposes to address the
95 problem of the characterisation of the radiation force and especially the one exerted by
96 acoustic tweezers, it is reasonable to validate the methodology on a field as close as possible
97 to the final target. The BSC for a focused vortex beam are⁵:

$$A_n^m = \delta_{m,m'} 4\pi (kr_0)^2 h_n^{(1)}(kr_0) \int_{\pi-\alpha_0}^{\pi} P_n^{m'}(\cos\theta') N_n^{m'} d\theta'. \quad (6)$$

98 with $\delta_{m,m'}$ the Kronecker delta, $h_n^{(1)}$ the spherical Hankel function of first kind, m' the
99 topological charge of the vortex and α_0 , a_0 , r_0 are respectively the aperture half angle, the
100 radius of the transducer and the focal distance as illustrated on top of Fig. 1. In this paper,

101 we use the expression of normalized spherical harmonics with a factor N_n^m (see Eq. 5), hence
 102 A_n^m are different from previous works^{6,5}.

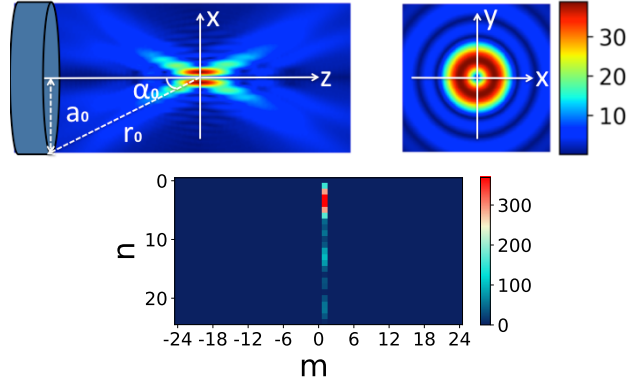


FIG. 1. (Top) Modulus of the complex pressure field at frequency corresponding to a wavelength of $1.25mm$ in water, and (bottom) BSC, for a focused vortex with topological charge $m' = 1$ the spherical basis is centered at the focus of the incident beam (color online)

103 Using Eq. 4, the pressure field can be computed anywhere. Fig. 1 shows the pressure
 104 field for a focused vortex beam of charge $m' = 1$ (top row), and the BSC (bottom). We
 105 selected the case of water, $c_0 = 1500m \cdot s^{-1}$, as propagating medium and a frequency of
 106 $1.2MHz$. The wavelength is $\lambda = 1.25mm$. The pressure field has a zero amplitude along
 107 the axis of propagation. This is a common feature associated with vortex beam^{19,26}. The
 108 focusing is sharp because the aperture of the transducer is $110mm(88\lambda)$, $75mm(60\lambda)$ away
 109 from the focus (corresponding to an aperture half angle equal to $\alpha_0 = 43^\circ$). As expected
 110 the BSC are restricted to the column $m = 1$ with a non intuitive variation in function of
 111 the radial degree. We assessed numerically the error on the radiation force, Eq. 1-3 by

112 decreasing the truncation order. Thereafter, all series are truncated at $n \leq N = 25$ and the
 113 error on the force is 0.001.

114 **A. Lebedev Quadrature**

115 The first method is based on the orthogonality of the spherical harmonics: $\langle Y_n^m, Y_{n'}^{m'} \rangle =$
 116 $\delta_{n,n'}\delta_{m,m'}$ where the scalar product on the sphere is defined by $\langle f(\theta, \varphi), g(\theta, \varphi) \rangle =$
 117 $\int \int f(\theta, \varphi)g(\theta, \varphi) \sin \theta d\theta d\varphi$. By applying this property, BSC A_n^m can be expressed by inte-
 118 grals over a spherical surface:

$$\begin{aligned}
 A_n^m &= \frac{1}{p_0 j_n(kr)} \langle p, Y_n^m \rangle \\
 &= \frac{1}{p_0 j_n(kr)} \int_{\theta} \int_{\varphi} p(\theta, \varphi) Y_n^{m*}(\theta, \varphi) \sin \theta d\theta d\varphi.
 \end{aligned}
 \tag{7}$$

119 The integrals in Eq. 7 are computed by numerical integration. Using a numerical quadra-
 120 ture to perform this integration in the context of acoustic radiation force or torque have
 121 already been investigated^{17,18}. In these previous works, the sphere was sampled with a very
 122 fine grid incompatible with actual measurements of the pressure fields and there was no
 123 noise. Different quadrature rules have been tested: Legendre-Gauss quadrature, Chebyshev
 124 quadrature¹⁰ and Lebedev quadrature. Among these quadratures, the Lebedev quadrature³¹
 125 gives the best precision for a given number of points and only that quadrature is used here²¹.
 126 The number, position and the weight of Lebedev grids defined on an unit sphere $((x_i, y_i, z_i)$
 127 and weights w_i) have been derived by Sobolev³¹. Therefore, measuring the pressure field at
 128 the Lebedev points (see Fig. 2 to visualize their positions) and using this quadrature give

129 the BSC A_n^m .

$$A_n^m = \frac{1}{p_0 j_n(kr)} \sum_{i=0}^{I-1} p(\theta_i, \varphi_i) Y_n^{m*}(\theta_i, \varphi_i) w_i. \quad (8)$$

130 Lebedev quadrature has optimal efficiency, i.e. the number of points required, $I =$
131 $(\mathcal{N} + 1)^2/3$, is the smallest, where \mathcal{N} is the highest order of the polynomials integrated on
132 the sphere. Moreover, the distance between the Lebedev points is roughly constant. This
133 feature is very interesting since it provides an optimal sampling of the sphere in regards
134 with the finite size of an hydrophone and thus it optimizes the signal-to-noise-ratio (SNR)
135 The integrand is the product of spherical harmonics, Eq. 4, 7. If the series is truncated at
136 $n \leq N$, the integrand is a polynomial of order smaller than $2N$ and hence $\mathcal{N} = 2N$. For our
137 case, $N = 25$ and this yields $I = 867$. It must be noted that the number of Lebedev points
138 is not arbitrary. Here, we use $I = 974$ Lebedev points on a sphere with radius $7mm(5.6\lambda)$.
139 This choice allows to perfectly retrieve the high order modes (here up until $n = 25$) as
140 shown in Fig. 2, the BSC obtained by the Lebedev quadrature for a focused vortex beam. Of
141 course, this previous estimation does not take into account the noise in the measurements.
142 It is known that the determination of the BSC are prone to errors in the presence of noise²⁹.
143 To assess the robustness of the method in presence of noise, we proceed in three steps. First,
144 the BSC of Eq. 6, named thereafter A_{nth}^m , are computed and the corresponding pressure field
145 calculated with Eq. 4 on the Lebedev grid and in the focal plane to determine the maximum
146 pressure. Second, a noise with a uniform distribution in an interval of amplitude 5% of this
147 maximum pressure is added to the pressure field calculated on the Lebedev grid. Third, the
148 BSC of this noisy pressure field, noted A_n^m , are estimated with Eq. 8 and shown on Fig. 2.
149 In Fig. 2, the lines where the BSC are very different from the original ones correspond to

150 the values closest to zero for the Bessel function (Fig. 3). Indeed, since the scalar product
 151 with spherical harmonics is a linear operation, the result is the scalar product with the ideal
 152 pressure fields plus the scalar product with the noise. Hence the error is proportional to
 153 $1/j_n(kr)$. On Fig. 3, we can observe a first oscillating part up to $n = 35$ followed by a fast
 154 decrease converging to 0. We selected a sphere radius large enough, $7mm(5.6\lambda)$, so that the
 155 truncature order $N = 25$ is located in the oscillating part.

156 To assess the numerical performance of the method, we compute the relative error:

$$err = \frac{1}{(N+1)^2} \sum_{n=0}^N \sum_{m=-n}^{m=n} \frac{|A_n^m - A_{nth}^m|}{max(|A_{nth}^m|)} \quad (9)$$

157 $(N+1)^2$ is the total number of BSC A_n^m of order $n \leq N$. Here the relative error is 0.061.

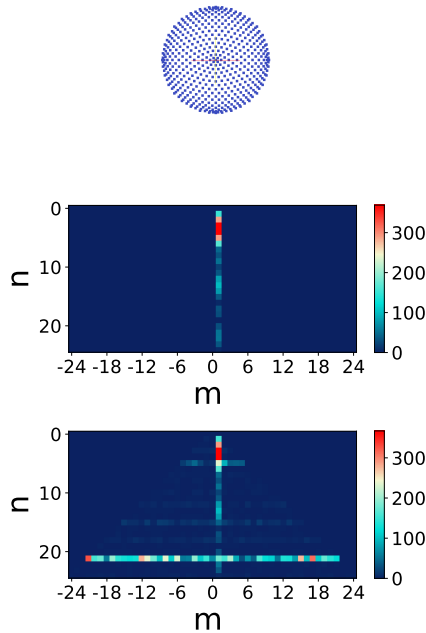


FIG. 2. (Top) points on a Lebedev sphere, and (Middle) reconstructed BSC for an incident focused vortex beam without noise and (Bottom) with 5% noise. (color online)

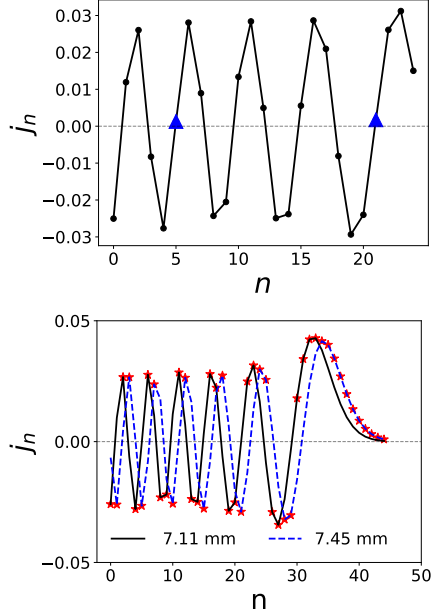


FIG. 3. (Top) Amplitude of the spherical Bessel $j_n(kr)$ function for a radius $r = 7mm(5.6\lambda)$ (the blue triangles show the values close to zero) and (Bottom) for two different radii $r_1 = 7.11mm(5.7\lambda)$ and $r_2 = 7.45(6\lambda)$ (the red points show the maximum values between $|j_n(kr_1)|$ and $|j_n(kr_2)|$ for each order n). The frequency is $f_0 = 1.2MHz$. (color online)

158 An upgrade in order to mitigate the detrimental effect of noise is to use a double layer
159 Lebedev sphere²⁹. The idea is to use two spheres with different radii and to apply the
160 Lebedev quadrature, for a given order n , to the sphere for which the Bessel function has
161 the greatest absolute value. Using the asymptotic behavior of Bessel function for large x
162 compared to n , $j_n(x) \approx \cos(x - \pi/2)/x$, in Fig. 3, we selected the radius of the second
163 sphere such that $j_n(x') \approx \sin(x' - \pi/2)/x'$ to optimize the estimation, this leads to $r_1 =$
164 7.11 mm(5.7λ) and $r_2 = 7.45$ mm(6λ). The red stars indicate the chosen value between the
165 two Bessel functions to compute the BSC of order n . The double layer Lebedev sphere grids
166 are presented in Fig. 4. For each sphere, 974 Lebedev points are used. Fig. 4 shows the

167 BSC obtained with this method. They are close to the original ones (Fig. 1) and the relative
 168 error decreases from 0.06 to 0.015. Nevertheless, one can see that the BSC for $m \neq 1$ are
 169 not strictly equal to zero and thus a weak error remains on the estimated BSC.

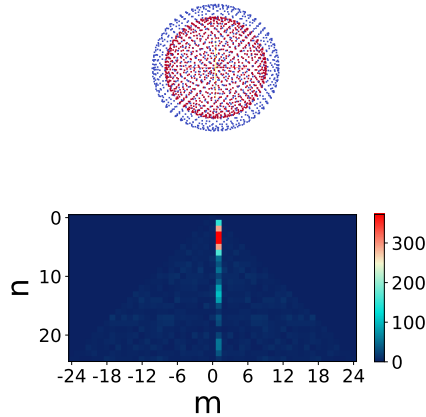


FIG. 4. (Top) measurement points of a double layer Lebedev sphere, (Bottom) reconstructed BSC for an incident focused vortex beam with 5% noise by the double layer Lebedev quadrature method. (color online)

170 B. Regularization of the inverse problem by a sparse method

171 Instead of solving Eq. 7 with its discretized version Eq. 8, another strategy consists
 172 in solving Eq. 4 whose discretized counterpart can be reformulated under a matrix/vector
 173 form:

$$\underline{P} = \underline{\underline{M}}\underline{A} + \underline{\epsilon}. \quad (10)$$

174 with vector \underline{P} whose components are the Fourier transform of the pressure field at frequency
 175 f_0 at points of discretization $(x_i, y_i, z_i) : \hat{p}(x_i, y_i, z_i, f_0)$ of length I , vector \underline{A} whose compo-

176 nents are the BSC $A_l = A_n^m$ with $l = n(n + 1) + m$ of length $L = (N + 1)^2$, the matrix $\underline{\underline{M}}$
177 whose elements are $(j_n(kr_i)Y_n^m(\theta_i, \varphi_i))$ with $(r_i, \theta_i, \varphi_i)$ the points (x_i, y_i, z_i) written in spheri-
178 cal coordinates of size $(I \times L)$ and vector $\underline{\epsilon}$ the additive noise on points (x_i, y_i, z_i) . To compare
179 this method with the double layer Lebedev sphere quadrature, we set the same number of
180 points: 1948 dispersed in a spherical volume of identical radius $r = 7.11mm(5.7\lambda)$. As
181 previously, the truncature order is set to 25. At this stage the points distribution is free and
182 this can be used to avoid an ill-conditioned matrix. Then, the best choice is a set of random
183 points distributed in a spherical volume as illustrated on Fig. 5.

184 Because of the noise, the matrix $\underline{\underline{M}}$ is always full rank, the direct inversion is then always
185 possible but unstable in regard of a small change in the noise. This ill-posed problem required
186 regularization to get a meaningful solution. As can be seen on Fig. 1 for a focused vortex
187 beam, a large number of BSC are null. So, vector \underline{A} is sparse. This *a priori* can be used to
188 regularize the inversion:

$$\tilde{\underline{A}} = \operatorname{argmin} \|\underline{A}\|_0 \text{ such as } \underline{P} = \underline{\underline{M}}\underline{A} \quad (11)$$

189 With this formulation, vector $\tilde{\underline{A}}$ is searched with a particular constraint: it must contain a
190 minimum of non-zero terms.

191 To solve Eq. 11, we choose to use Orthogonal Matching Pursuit algorithm (OMP)¹¹.
192 This algorithm is iterative. For each iteration, the component of $\underline{\underline{M}}$ with the highest inner
193 product with the remaining part of vector \underline{P} is selected. Then its contribution is subtracted
194 and the iterations continue on the residue. This procedure stops when the iteration reaches
195 the number of non-zero elements of the BSC (25 in our case) or when the residual reaches
196 a limit.

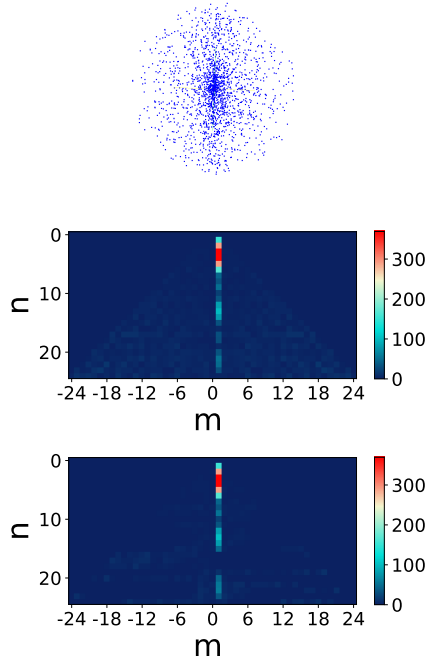


FIG. 5. (Top) randomly distributed measurement points in a sphere, and (Middle) reconstructed BSC for an incident focused vortex beam with 5% noise by the OMP method and (Bottom) block-OMP method. (color online)

197 With the OMP method, we should be able to recover the BSC on the column $m = 1$ with
 198 25 iterations. However, tests for a vortex beam have shown the inefficiency of this stopping
 199 criterion. Thus, the stopping criterion of the OMP procedure will be the residual limit
 200 (lower than 0.001). Fig. 5 shows the BSC obtained with the OMP algorithm for the same
 201 noisy pressure field as before. There is a very good agreement with the original set of BSC
 202 even if some BSC laying outside the column $m = 1$ are not exactly set to zero. Here, the
 203 relative error is 0.0141 close to the 0.015 obtained with the Lebedev method. A drawback is
 204 the number of iteration required, the computation can be very long. A method to improve
 205 this is the Block version of OMP. It's the same procedure but with the matrix $\underline{\underline{M}}$ in a block

206 version¹⁵. Fig. 5 shows the BSC obtained by applying the Block-OMP method, the matrix
 207 $\underline{\underline{M}}$ is divided into blocks of $(N \times 10)$, and the iteration number is 35 only. An unexpected
 208 result is that the relative error is then twice better : 0.006

209 C. Angular spectrum method (ASM)

210 A third approach is to use a transformation from angular spectrum to spherical harmonics.³⁰.
 211 The Fourier transform of the pressure in plane z can be seen as a superposition of plane
 212 waves:

$$\hat{p}(x, y, z, \omega) = \frac{1}{4\pi^2} \int \int_{k_x^2 + k_y^2 \leq k^2} S(k_x, k_y) e^{ik_x x + ik_y y + i\sqrt{k^2 - k_x^2 - k_y^2} z} dk_x dk_y, \quad (12)$$

213 where the angular spectrum $S(k_x, k_y)$ is the 2D spatial Fourier transform of the pressure
 214 in plane $z = 0$:

$$S(k_x, k_y) = \int_{-\infty}^{+\infty} \int_{-\infty}^{+\infty} \hat{p}(x, y, z = 0, \omega) e^{-i(k_x x + k_y y)} dx dy, \quad (13)$$

215 According to³⁰, the pressure field can be rewritten:

$$\hat{p}(x, y, z, \omega) = \frac{1}{\pi} \sum_{n=0}^{\infty} i^n j_n(kr) \sum_{m=-n}^n Y_{nm}(\theta, \varphi) \int \int_{k_x^2 + k_y^2 \leq k^2} S(k_x, k_y) Y_{nm}^*(\theta_k, \varphi_k) dk_x dk_y, \quad (14)$$

216 with: $k_x = k \sin(\theta_k) \cos(\varphi_k)$ $k_y = k \sin(\theta_k) \sin(\varphi_k)$ and $k_z = k \cos(\theta_k)$. The comparison of
 217 Eq. 4 and Eq. 14 shows that the A_n^m can be written as:

$$A_n^m = \frac{i^n}{\pi} \int \int_{k_x^2 + k_y^2 \leq k^2} S(k_x, k_y) Y_{nm}^*(\theta_k, \varphi_k) dk_x dk_y. \quad (15)$$

218 The noisy pressure field is simulated here on a square grid of dimension $7mm \times$
 219 $7mm(5.6\lambda \times 5.6\lambda)$ regularly sampled with a total of 2500 points. Note that the mesh

220 grids of ASM should be very fine otherwise errors of integration in Eq. 15 arise. The square
 221 grid is located at the focal distance $(x, y, z = 0)$. This field is Fourier transformed (Eq.
 222 13) with a discrete Fourier transform (DFT). The sampling after a DFT can be refined
 223 by zero-padding for instance. We performed a polynomial interpolation instead. Indeed,
 224 knowing the polynomial coefficients, numerical integration of Eq. 15 can be achieved with
 225 a variable step method to increase accuracy.

226 Fig. 6 shows the BSC obtained with the ASM method. The agreement with the original
 227 BSC is quite good especially for column $m = 1$. Nevertheless, other columns contain non
 228 null BSC with a relative important amplitude. The relative error is 0.014.

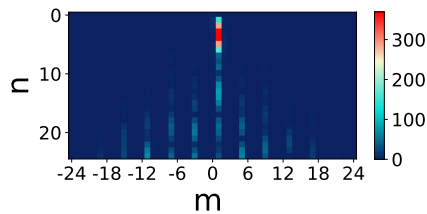


FIG. 6. Computation of the BSC by angular spectrum decomposition. (color online)

229 Therefore, all methods except the Lebedev quadrature on a single sphere allow to retrieve
 230 the BSC for a focused vortex beam with a good confidence even in presence of noise. The
 231 results are synthesized in Tab. I.

232 D. Estimation of the radiation pressure by the three methods

233 To assess the efficiency of each method, we calculate the radiation forces exerted on a
 234 polystyrene sphere of radius $r = 0.1\lambda$ using equations 1, 2, 3. These forces are then decom-

Methods	Relative Error
Lebedev quadrature (Single sphere)	0.061
Double layer Lebedev quadrature	0.015
OMP	0.014
Block - OMP	0.006
ASM	0.014

TABLE I. Relative error for three methods

235 posed into three components: radial, azimuthal and axial forces (F_ρ, F_ϕ, F_z) in a cylindrical
 236 basis (ρ, ϕ, z) . On the left of Fig. 7, the forces are calculated by using all the BSC obtained
 237 by the three methods, while on the right of Fig. 7, the forces are computed with A_n^1 only.
 238 All methods yield accurate estimations of the radial force. On the contrary, the azimuthal
 239 force, F_ϕ , has a much weaker amplitude and all methods give poor estimates. Nevertheless,
 240 OMP method roughly recovers the original shape of the force. These differences originate
 241 from the estimated BSC with finite value outside column $m = 1$. It is shown in Fig. 7 that
 242 after filtering out these BSC, all methods recover perfectly the theoretical force. In the case
 243 of the axial force, F_z , both OMP and the ASM turn out to provide good estimations while
 244 again, the Lebedev method is less efficient and leads to fast oscillations around the expected
 245 curve. However, these errors can not be reduced by filtering BSC outside $m = 1$. We may
 246 assume that the error is hidden in column $m = 1$.

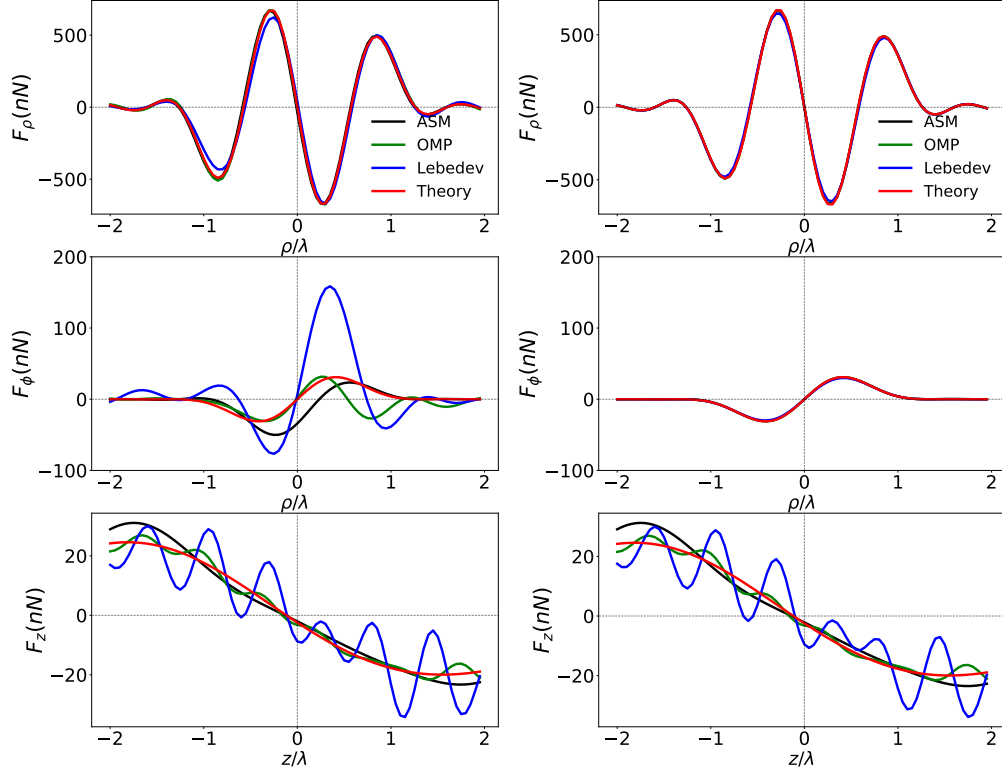


FIG. 7. (Left) radiation force exerted on a polystyrene sphere of radius $r = 0.1\lambda$ with all the BSC, and (Right) with only BSC on column $m = 1$. (color online)

247 The oscillations on the axial force calculated by Lebedev method are periodical, similar
 248 to those caused by a standing wave. Moreover, we know that the radiation pressure due to
 249 a standing wave is much stronger than the one due to a progressive wave²⁰. Any error on
 250 the estimated BSC in this regard should lead to large discrepancies on the force estimation.
 251 In order to investigate this assumption, a weak amplitude wave propagating in the opposite
 252 direction is superposed to the incident wave. The BSC of the counter propagating wave can
 253 be computed as follow. The symmetry $z \rightarrow -z$ transforms $\cos(\theta)$ into $\cos(\pi - \theta) = -\cos(\theta)$.
 254 Then, considering that the associated Legendre functions $P_n^m(\cos(\theta))$ satisfy the relation :

$$P_n^m(-x) = (-1)^{(n+m)} P_n^m(x). \quad (16)$$

255 and Eq. 4, 5, the BSC of the wave propagating in the opposite direction can be computed
 256 by multiplying the BSC by $(-1)^{(n+m)}$. Taking into account the mean relative error on the
 257 estimated BSC 0.006 for block OMP, we fixed the amplitude of this weak counterpropagating
 258 wave at 0.005 so that the new BSC are $(1 + 0.005(-1)^{(n+m)})A_{nth}^m$. On Fig. 8 is plotted the
 259 axial force for the progressive wave only and with the counterpropagating wave superposed.
 260 Comparing with Fig. 7, oscillations with the same periodicity but weaker amplitudes are
 261 obtained.

262 There remains to explain why the Lebedev method is more sensitive to the noise than the

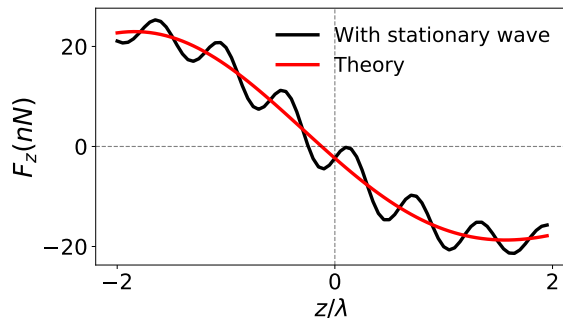


FIG. 8. Axial force exerted on a polystyrene sphere of radius $r = 0.1\lambda$ with theoretical BSC A_n^m (black) and theoretical BSC with a counter propagating wave with 0.5% amplitude (red). (color online)

263

264

265 other two methods. In our simulation, the random noise amplitude is evenly distributed
 266 between -5% and 5% of the maximum pressure of the incident beam in all three cases.
 267 However for Lebedev quadrature, the pressure field is sampled at the surfaces of two spheres
 268 with radius $r = 7.11mm(5.7\lambda)$ and $r = 7.45mm(6\lambda)$ where the wave is either yet converging,
 269 $z < 0$, or diverging, $z > 0$. Since the wave is sharply focused, on these spheres its amplitude

270 and hence the SNR is $10dB$ lower. On the contrary, the set of points used either inside a
 271 spherical volume (OMP) or on a focal plane (ASM) contains locations where the pressure
 272 amplitude is maximum. By calculating the SNR at a measurement point where the signal
 273 is the maximum for each method, we obtain the results of $22.5dB$, $32.2dB$ and $32.5dB$ for
 274 the Lebedev quadrature, OMP and ASM respectively. To confirm the role played by the
 275 SNR, the OMP method is now applied in conditions similar to the ones used for Lebedev
 276 quadrature. The pressure field is sampled on a set of points randomly distributed on a
 277 spherical surface of $r = 7mm(5.6\lambda)$. The axial force obtained by the two methods are
 278 now similar with oscillating errors of about the same period and amplitude. Besides, if we
 279 increase the radius to $10mm(8\lambda)$, the fluctuations become stronger as expected since the
 280 SNR is even more degraded.

281 To compare the numerical estimation of the forces by different methods (with all the BSC

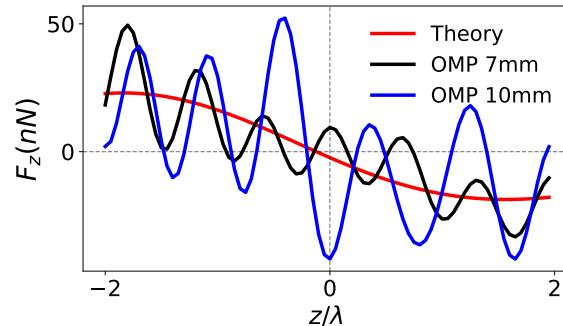


FIG. 9. Axial force exerted on a polystyrene sphere of radius $r = 0.1\lambda$ with BSC computed by
 OMP method on two spherical surfaces (black and blue) and the theoretical force (red). (color
 online)

282

283

284 A_n^m), the relative errors between the force calculated with the A_n^m , F , in the presence of

285 noise and the force computed with the A_{nth}^m , F_{th} , are then calculated :

$$err_{force} = \frac{1}{K} \frac{\sum_0^K |F - F_{th}|}{max|F_{th}|} \quad (17)$$

286 K is the total number of positions where the forces are estimated. The results are presented
 287 in Tab. II. We can conclude that both the OMP and angular spectrum are effective methods
 288 for estimating the radiation force from pressure field measurements with very low relative
 289 error as presented in Tab. II. The task is nevertheless difficult since small errors potentially
 290 result in spurious standing waves and the radiation pressure exerted by standing waves is
 291 much stronger than for progressive waves.

Relative error	Lebedev	OMP	ASM
F_ρ	0.036	0.012	0.018
F_ϕ	0.87	0.23	0.22
F_z	0.29	0.056	0.096

TABLE II. Relative error of the forces for three methods

292 IV. EXPERIMENTAL MEASUREMENTS

293 In this section, the three methods are applied on experimental data. A focused Gaus-
 294 sian beam, with charge $m' = 0$, and a focused vortex beam with charge $m' = 1$ have been
 295 synthesized using a large antenna made of 120 piezoelectric transducers distributed on a
 296 hexagonal pattern on a concave surface with a radius of curvature of $45cm$. The array aper-
 297 ture is $11cm(88\lambda)$. An acoustic lens is used to reduce this focal to $7.5cm(56\lambda)$. With the

298 lens, the half-angle, α_0 , is comparable to the simulated cases. The pressure field is synthe-
 299 sized by selecting the electric signals fed to each transducers by a multichannel electronics
 300 made of 120 arbitrary signals generators. These signals are calculated using the inverse
 301 filter technique^{26,27,33}. The set-up and procedure are identical to the ones used in previous
 302 work⁷. The incident sound beam was then measured by a calibrated needle hydrophone of
 303 $0.2mm(0.2\lambda)$ diameter (Precision Acoustics Ltd, UK) on three different grids corresponding
 304 to the different algorithms presented in the previous section. The measurement grids are
 305 all centered on the focal point of the vortex beam. For each location of the hydrophone, an
 306 ultrasound burst of 10 cycles is repeated 128 times and the records are averaged to increase
 307 the SNR. The experimental SNR is $20dB$ lower than the SNR in the previous section. After
 308 these measurements on the different grids, we apply the three methods described in sec-
 309 tion II to estimate the BSC. The obtained BSC completely describe the field, Eq. 4. We
 310 measured the acoustic pressure on the transverse plane (xy) (on the ASM grid) and the
 311 vertical plane (xz) (on a rectangular grid of dimension $7mm \times 20mm$ ($5.6\lambda \times 16\lambda$) with
 312 steps of $0.4mm \times 0.3mm$ ($0.3\lambda \times 0.2\lambda$)). A DFT is then used to get the measured pres-
 313 sure in the Fourier domain and then extract the modulus at $1.2MHz$. Fig 10 displays the
 314 computed and measured modulus of the pressure field at this frequency. The reconstructed
 315 fields computed with the three different methods are in very good agreement with the direct
 316 measurements. On the lateral, (xy) , plane. The main lobe is perfectly recovered and in the
 317 case of the vortex beam the small anisotropy on the bright ring is accurately estimated.
 318 The secondary ring of high pressure modulus characteristic of diffraction by a truncated
 319 aperture, i.e. the array of transducers, is also efficiently estimated. Compared to simulated
 320

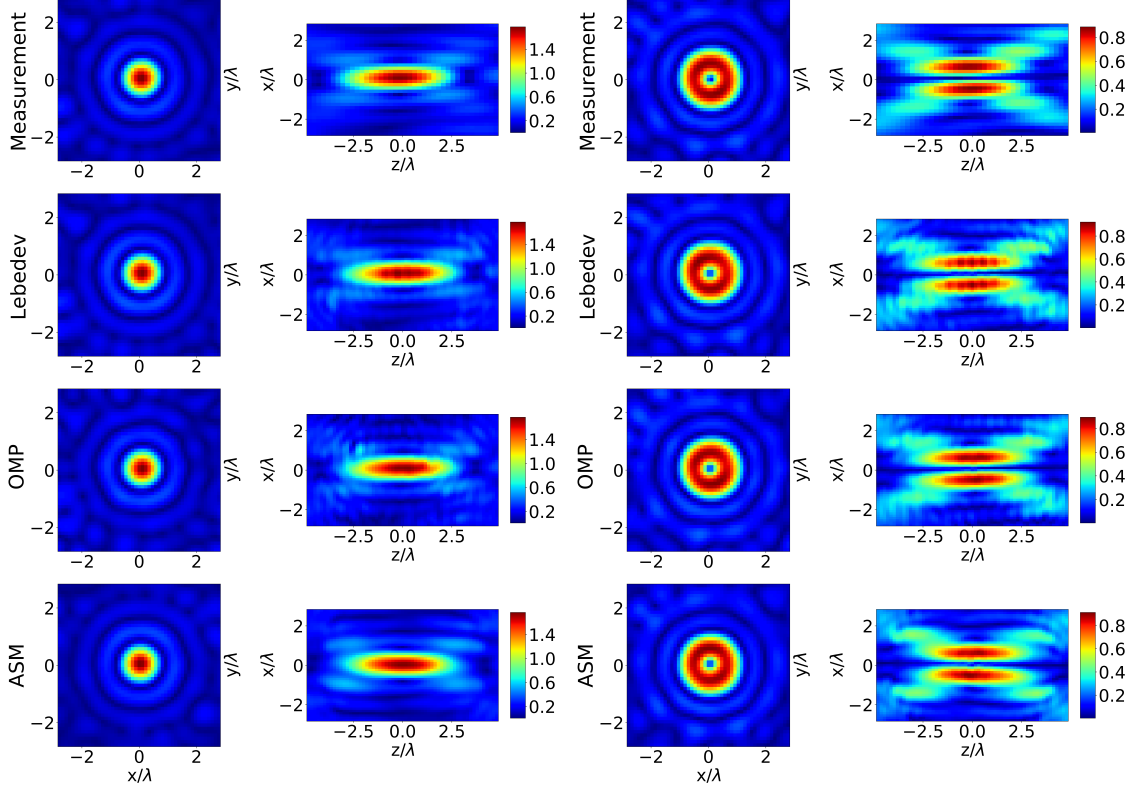


FIG. 10. Reconstruction of the incident beam in Fourier domain, (pressure modulus is shown), for the focused Gaussian beam (Left), and the focused vortex beam with $m' = 1$ (Right). (color online)

321 results of the previous section, the noise is not the single source of discrepancy between A_n^m
 322 and A_{nth}^m and as consequence between F and F_{th} , Eq. 17. The inverse filtering while very
 323 efficient does not achieve a perfect synthesis of the looked for pressure fields, Fig 10. For
 324 instance, the experimental measurements are not perfectly axisymmetric and this will have
 325 an impact on the azimuthal force. For the axial plane, (xz) , OMP and ASM methods also
 326 provide quite a good reconstruction on main and secondary lobes. The "X-shape" and high
 327 pressure at the focus, features expected for sharply focused beam, are perfectly reproduced,
 328 while the Lebedev quadrature estimation has some spurious amplitude oscillations. These

329 oscillations have a comparable period with the one observed on the axial force, F_z , Fig. 7,
 330 in the numerical simulation when noise was present. We provided an explanation for this
 331 phenomenon in the previous section. As a result, both the OMP and ASM are able to es-
 332 timate the incident BSC A_n^m and hence the acoustic pressure field in the volume of interest
 333 around the focus.

334 Finally, we use these obtained BSC of the focused Gaussian beam and the vortex beam
 335 $m' = 1$ to calculate the radiation forces exerted on polystyrene spheres of radius $r = 0.1\lambda$
 336 with Eq. 1, 2, 3. The results are shown on Fig. 11 and Fig. 12. The axial force obtained
 337 with Lebedev method is not presented on the Figures since it's very fluctuating like its re-
 338 construction on (xz) plane. As in the previous section, the relative error of the experimental
 339 forces for Gaussian beam and vortex are calculated and reported in tables Tab.III, IV.

Relative error	Lebedev	OMP	ASM
F_ρ	0.036	0.036	0.012
F_z	0.23	0.11	0.07

TABLE III. Relative error of the experimental forces for three methods (Gaussian beam)

340

341

342 According to Fig. 11, for a focused Gaussian beam and for each method the radial force is
 343 in good agreement with the theoretical one. Theoretically no azimuthal force is applied, but
 344 a weak rotational force exists in the force estimation by three methods. This dissimilarity of
 345 azimuthal force can be due to the difference between the theoretical and experimental field
 346 synthesised by inverse filtering, as well as the presence of the noise in the measurements. As

Relative error	Lebedev	OMP	ASM
F_ρ	0.027	0.057	0.034
F_ϕ	0.71	0.6	0.99
F_z	0.8	0.14	0.14

TABLE IV. Relative error of the experimental forces for three methods (Acoustic vortex $m' = 1$)

347 for the axial force, the force estimated by ASM is very close to the theoretical one with a very
348 low relative error of 0.07. However, the one calculated by OMP appears to be oscillating
349 though in the reconstruction on plane (xz) no oscillations are visible. Note that the trap
350 slope is positive for both radial and axial forces. Therefore at the origin the force is null but
351 the equilibrium is unstable. To achieve acoustical tweezers for a stiffer and denser particle
352 compared to water, cancellation of the pressure field at the focus is required as the case
353 studied below.

354 For the focused vortex beam of charge $m' = 1$, the forces are quite similar with the ones
355 obtained by adding noise in the numerical assessment of the three methods (see previous
356 section). First, the computation of the radial force agrees with the theoretical force whatever
357 the method. Secondly, the azimuthal forces computed by the experimental BSC are different
358 from the theoretical one. These differences are caused by the value of A_n^m coefficients outside
359 column $m = 1$. If we keep only column $m = 1$ and recalculate the azimuthal force, then, all
360 the forces for different methods superpose with the theoretical force. This filtering makes
361 the pressure modulus axisymmetric and eliminates any anisotropy in the transverse plane

362 whatever its origin inverse filtering imperfection or biased estimation of BSC. The third
363 observation is that both OMP and ASM provide a good estimate of the axial force which
364 has the same negative slope as the theoretical one, i.e same trap strength and stiffness. The
365 OMP axial force has some fluctuations, but performs much better than the Lebedev method,
366 the force obtained with ASM is smooth and close to the theory but with a shift about 0.2λ
367 of the equilibrium position where $F_z = 0$. This shift can be caused by a slight shift 0.2λ
368 ($0.25mm$) of the focal point in the experimental measurements. As reported in the Tab. IV,
369 even with this shift, the relative error is small (0.14), by cancelling the shift, the relative
370 errors will decrease to 0.091 and 0.085 for the OMP and ASM respectively which are very
371 similar to the numerical estimations in the Tab. II of section III.

374 V. CONCLUSION

375 In this paper, the measurement of the radiation pressure on an elastic sphere exerted by
376 acoustic tweezers is presented. The radiation force is not measured directly but is obtained
377 from measurements of the pressure field associated with a model (see Eqs.1-3). To obtain the
378 forces, it is necessary to estimate the BSC from experimental sampling of the pressure field.
379 Three methods were developed in section III: the Lebedev double layer sphere quadrature,
380 the OMP method, and the ASM. First, we assessed the methods by simulating an acoustic
381 vortex of charge $m' = 1$ with 5% noise. The results show that all these methods can recover
382 the BSC. In spite of that, the forces computed by the different methods agree well with the
383 theory, except the Lebedev quadrature for which the axial force is fluctuating.
384 The experimental verification of these methods is done in section IV. Compared with the

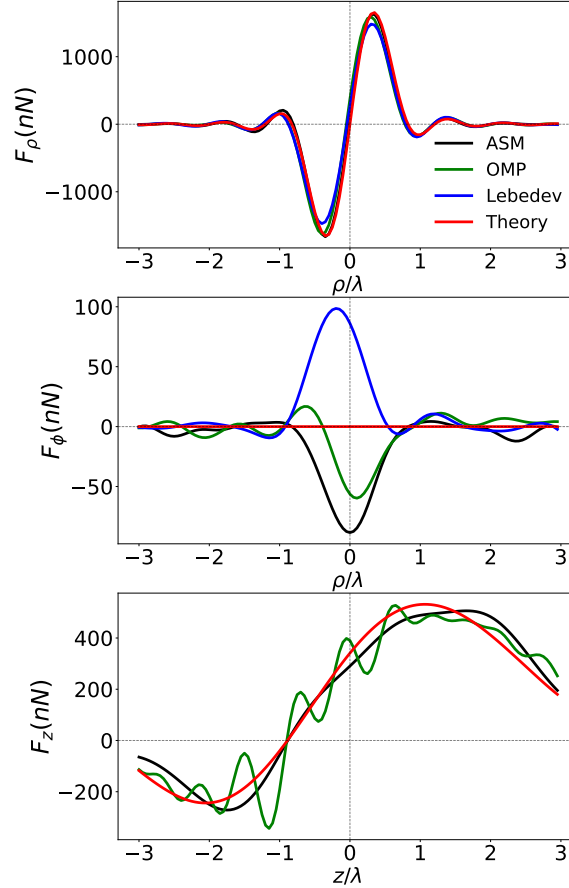


FIG. 11. Experimental radial F_ρ , azimuthal F_ϕ and axial F_z forces exerted on an polystyrene sphere of radius $r = 0.1\lambda$ in a focused Gaussian beam with charge $m' = 0$. (color online)

385 measurements in (xy) plane, the reconstructions of the field by the three methods are similar
386 and almost identical. Nevertheless, for (xz) plane reconstructions, the field rebuilt by the
387 Lebedev quadrature contains a lot of oscillations. Apart from that, both the OMP method
388 and the angular spectrum method are in good agreement with the experimental data. From
389 the analysis of the forces, the OMP and angular spectrum (ASM) methods allow to pre-
390 dict the radial and axial forces with a good precision and the azimuthal force with a lower

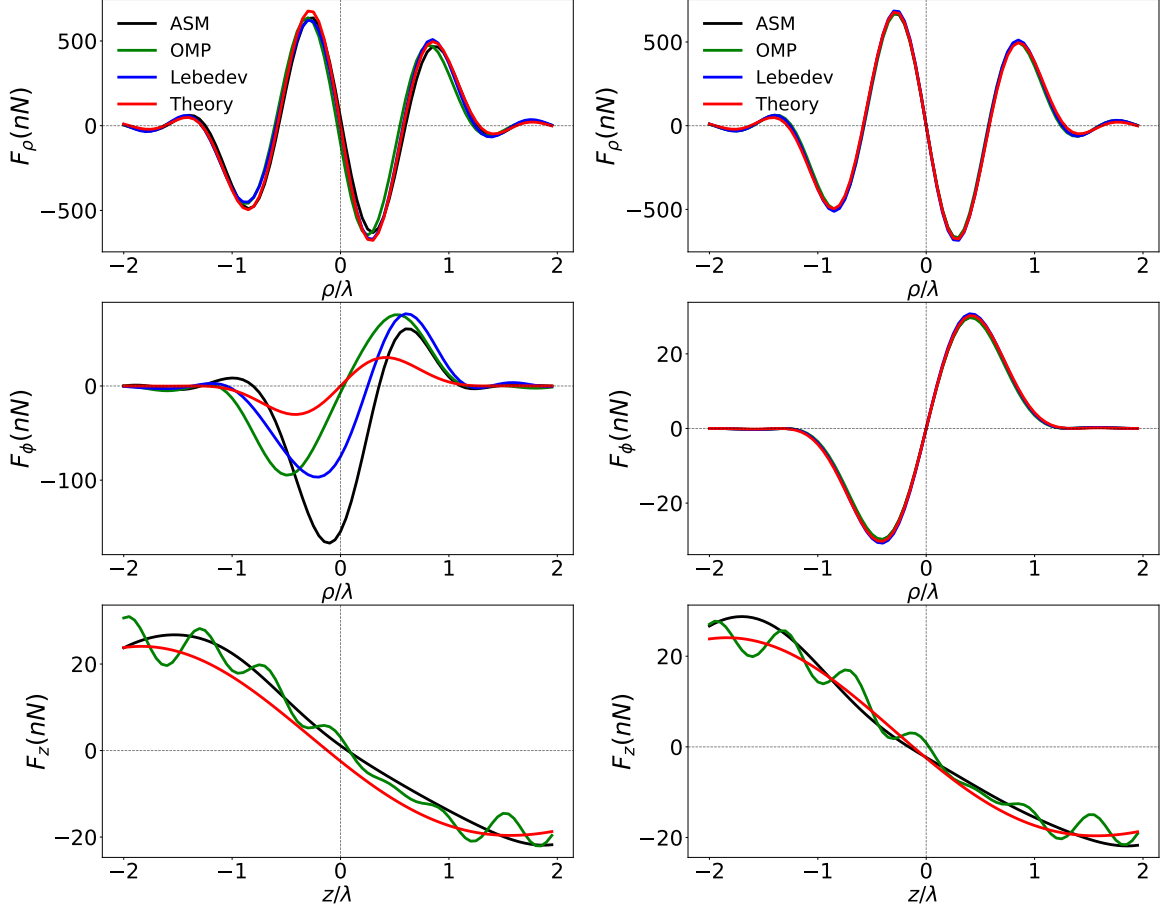


FIG. 12. Experimental radial F_ρ , azimuthal F_ϕ , axial F_z forces exerted on an polystyrene sphere of radius $r = 0.1\lambda$ in a focused vortex beam with charge $m' = 1$, calculated by the total coefficients (Left), and only by the BSC in column $m = 1$ (Right). (color online)

391 precision because it is sensitive to the noise outside column $m' = 1$ of the matrix of the BSC.

392

393 With the help of these methods, we are able to anticipate the radiation forces by mea-
 394 suring the acoustic field. As presented in previous sections, a very important component of
 395 three dimensional radiation force is the axial force which is much smaller than the transverse
 396 ones. In our experiments, we were capable to measure the axial force with a low relative

397 error of 0.14. For further measurements, this accuracy can be improved by increasing the
398 axial force, for example, in the case of an acoustic vortex we can increase the aperture angle
399 α_0 (Fig.1) to get larger axial forces. At the same time, reducing the noise by any methods:
400 shielding, averaging, filtering would help. The SNR leading to spurious standing wave is
401 the main limitation for axial or azimuthal force measurements.

402 ACKNOWLEDGMENTS

403 This work was supported by French state funds managed by the ANR within the In-
404 vestissements d’Avenir programme under reference ANR-11-IDEX-0004-02, and more specif-
405 ically within the framework of the Cluster of Excellence MATISSE led by Sorbonne Univer-
406 sités.

407 VI. REFERENCE

408 REFERENCES

- 409 ¹A. Ashkin. Acceleration and trapping of particles by radiation pressure. *Phys. Rev. Lett.*,
410 24(4):156, 1970.
- 411 ²A. Ashkin, J. M. Dziedzic, J.E. Bjorkholm, and S. Chu. Observation of a single-beam
412 gradient force optical trap for dielectric particles. *Opt. Lett.*, 11(5):288–290, 1986.
- 413 ³A. Ashkin, J. M. Dziedzic, and T. Yamane. Optical trapping and manipulation of single
414 cells using infrared laser beams. *Nature*, 330(6150):769, 1987.

- 415 ⁴D. Baresch. *Acoustic tweezers: trapping and manipulation of an object by radiation pressure*
416 *of a progressive wave*. PhD thesis, Université Pierre et Marie Curie-Paris, Paris 6, 2014.
- 417 ⁵D. Baresch, J-L. Thomas, and R. Marchiano. Spherical vortex beams of high radial degree
418 for enhanced single-beam tweezers. *J. Appl. Phys.*, 113:184901, 2013.
- 419 ⁶D. Baresch, J-L. Thomas, and R. Marchiano. Three-dimensional acoustic radiation force
420 on an arbitrarily located elastic sphere. *J. Acoust. Soc. Am.*, 133(1):25–36, 2013.
- 421 ⁷D. Baresch, J-L. Thomas, and R. Marchiano. Observation of a single-beam gradient force
422 acoustical trap for elastic particles: acoustical tweezers. *Phys. Rev. Lett.*, 116(2):024301,
423 2016.
- 424 ⁸D. Baresch, J-L. Thomas, and R. Marchiano. Orbital angular momentum transfer to stably
425 trapped elastic particles in acoustical vortex beams. *Phys. Rev. Lett.*, 121(07):074301, 2018.
- 426 ⁹M. Baudoin, J-C. Gerbedoen, A. Riaud, O. Bou Matar, N. Smagin, and J-L. Thomas. Fold-
427 ing a focalized acoustical vortex on a flat holographic transducer: Miniaturized selective
428 acoustical tweezers. *Sci. Adv.*, 5:eaav1967, 2019.
- 429 ¹⁰Casper H. L. Beentjes. Quadrature on a spherical surface. *Working note available on the*
430 *website <http://people.maths.ox.ac.uk/beentjes/Essays>*, 2015.
- 431 ¹¹T. T. Cai and L. Wang. Orthogonal matching pursuit for sparse signal recovery with noise.
432 *IEEE T. Inform. Theory*, 57(7):4680–4688, 2011.
- 433 ¹²A. R. Carter, Y. Seol, and T. T. Perkins. Precision surface-coupled optical-trapping assay
434 with one-basepair resolution. *Biophys. J.*, 96(7):2926–2934, 2009.

- 435 ¹³D. J. Collins, C. Devendran, Z.C. Ma, J.W. Ng, A. Neild, and Y. Ai. Acoustic tweezers
436 via sub-time-of-flight regime surface acoustic waves. *Sci. Adv.*, 2(7):e1600089, 2016.
- 437 ¹⁴X.Y. Ding, Sz-Chin S. Lin, B. Kiraly, H.J. Yue, S.X. Li, I-K. Chiang, J.J. Shi, S. J Benkovic,
438 and T. J. Huang. On-chip manipulation of single microparticles, cells, and organisms using
439 surface acoustic waves. *P. Natl. Acad. Sci. USA*, 109(28):11105–11109, 2012.
- 440 ¹⁵Y. C. Eldar, P. Kuppinger, and H. Bolcskei. Block-sparse signals: Uncertainty relations
441 and efficient recovery. *IEEE T. Signal Proces.*, 58(6):3042–3054, 2010.
- 442 ¹⁶H. Goldstein, C. P. Poole, and J. L. Safko. *Classical Mechanics (3rd ed.)*. Addison-Wesley,
443 2001.
- 444 ¹⁷Silva G.T., Lopes J.H., and Mitri F. G. Off-axial acoustic radiation force of repulsor and
445 tractor bessel beams on a sphere. *IEEE T. Ultrason. Ferr.*, 60(6):1207–1212, 2013.
- 446 ¹⁸Silva G.T., Lobo T.P., and Mitri F.G. Radiation torque produced by an arbitrary acoustic
447 wave. *EPL*, 97:54003, 2012.
- 448 ¹⁹B. T. Hefner and P. L. Marston. An acoustical helicoidal wave transducer with applications
449 for the alignment of ultrasonic and underwater systems. *J. Acoust. Soc. Am.*, 106(6):3313–
450 3316, 1999.
- 451 ²⁰L. V. King. On the acoustic radiation pressure on spheres. *P. Roy. Soc. Lond. A Mat.*,
452 147(861):212–240, 1934.
- 453 ²¹V. I. Lebedev and D. N. Laikov. A quadrature formula for the sphere of the 131st algebraic
454 order of accuracy. In *Doklady Mathematics*, volume 59, pages 477–481. Pleiades Publishing,
455 Ltd.(,), 1999.

- 456 ²²J. Lee, C.Y. Lee, and K. K. Shung. Calibration of sound forces in acoustic traps. *IEEE*
457 *T. Ultrason. Ferr.*, 57(10):2305–2310, 2010.
- 458 ²³T. Lionnet, s. Joubaud, R. Lavery, D. Bensimon, and V. Croquette. Wringing out dna.
459 *Phys. Rev. Lett.*, 96(17):178102, 2006.
- 460 ²⁴A. H. Mack, D. J. Schlingman, L. Regan, and S. G. J. Mochrie. Practical axial optical
461 trapping. *Rev. Sci. Instrum.*, 83(10):103106, 2012.
- 462 ²⁵N. Malagnino, G. Pesce, A. Sasso, and E. Arimondo. Measurements of trapping efficiency
463 and stiffness in optical tweezers. *Opt. Commun.*, 214(1-6):15–24, 2002.
- 464 ²⁶R. Marchiano and J-L. Thomas. Synthesis and analysis of linear and nonlinear acoustical
465 vortices. *Phys. Rev. E*, 71(6):066616, 2005.
- 466 ²⁷R. Marchiano and J-L. Thomas. Doing arithmetic with nonlinear acoustic vortices. *Phys.*
467 *Rev. Lett.*, 101(6):064301, 2008.
- 468 ²⁸A. Marzo, S. A. Seah, B. W. Drinkwater, D. R. Sahoo, B. Long, and S. Subramanian.
469 Holographic acoustic elements for manipulation of levitated objects. *Nature comm.*, 6:8661,
470 2015.
- 471 ²⁹B. Rafaely. The spherical-shell microphone array. *IEEE T. Audio Speech*, 16(4):740–747,
472 2008.
- 473 ³⁰O. A. Sapozhnikov and M. R. Bailey. Radiation force of an arbitrary acoustic beam on an
474 elastic sphere in a fluid. *J. Acoust. Soc. Am.*, 133(2):661–676, 2013.
- 475 ³¹S. L. Sobolev. Cubature formulas on the sphere invariant under finite groups of rotations.
476 In *Selected Works of SL Sobolev*, pages 461–466. Springer, 2006.

- 477 ³²T. Strick, J-F. Allemand, D. Bensimon, and V. Croquette. Twisting and stretching single
478 dna molecules. *Prog. Biophys. Mol. Bio.*, 74(1-2):115–140, 2000.
- 479 ³³J-L. Thomas and R. Marchiano. Pseudo angular momentum and topological charge con-
480 servation for nonlinear acoustical vortices. *Phys. Rev. Lett.*, 91(24):244302, 2003.
- 481 ³⁴J. Wu. Acoustical tweezers. *J. Acoust. Soc. Am.*, 89(5):2140–2143, 1991.
- 482 ³⁵W.J. Xie, C.D. Cao, Y.J. Lü, Z.Y. Hong, and B. Wei. Acoustic method for levitation of
483 small living animals. *Appl. Phys. Lett.*, 89(21):214102, 2006.